Advances in Polyimide-Based Materials for Space Applications

Irina Gouzman, Eitan Grossman, Ronen Verker, Nurit Atar, Asaf Bolker, and Noam Eliaz*

The space environment raises many challenges for new materials development and ground characterization. These environmental hazards in space include solar radiation, energetic particles, vacuum, micrometeoroids and debris, and space plasma. In low Earth orbits, there is also a significant concentration of highly reactive atomic oxygen (AO). This Progress Report focuses on the development of space-durable polyimide (PI)-based materials and nanocomposites and their testing under simulated space environment. Commercial PIs suffer from AO-induced erosion and surface electric charging. Modified PIs and PI-based nanocomposites are developed and tested to resist degradation in space. The durability of PIs in AO is successfully increased by addition of polyhedral oligomeric silsesquioxane. Conductive materials are prepared based on composites of PI and either carbon nanotube (CNT) sheets or 3D-graphene structures. 3D PI structures, which can expand PI space applications, made by either additive manufacturing (AM) or thermoforming, are presented. The selection of AM-processable engineering polymers in general, and PIs in particular, is relatively limited. Here, innovative preliminary results of a PI-based material processed by the PolyJet technology are presented.

1. Introduction

Most of the materials development for the space industry took place in the 1960s, following the beginning of the space era in October 1957, when Sputnik ("Satellite I") was launched by the Soviet Union. Since then, space programs have developed in various directions and applications, including various Earth orbits and interplanetary missions. Earth orbits are categorized as low Earth orbit (LEO), at 200–800 km, geostationary Earth orbit (GEO), 36 000 km above the equator, and medium Earth orbit (MEO), which is between LEO and GEO.[1] Each orbit is intended for specific applications, such as communication, navigation, and Earth observation satellites.

Materials development is driven by performance improvement, weight reduction, and cost reduction. The key issues to be addressed, depending on a specific application, may include, among others, mechanical properties, weight, volatility, thermal stability, chemical reactivity, and, most importantly, durability in an anticipated space environment.

The effects of space environment on materials have been reviewed before.[2–6] Ground- and space-borne experiments have shown that prolonged exposure of spacecraft materials to the space environment leads to degraded thermal, electrical, mechanical, and optical systems performance, which can significantly affect the overall mission success, and possibly result in early mission failure.[1,2,7,8] Materials used in space are exposed to various hazards, including ultrahigh vacuum (UHV), ultraviolet (UV) radiation, ionizing radiation (namely, energetic electrons, protons, and heavy ions), as well as micrometeoroids and debris.[1–3] UHV introduces special concerns about outgassing of polymer-based materials. Outgassing gives rise to molecular contamination, an important phenomenon that can limit mission performance.[9] Atomic oxygen (AO) is an important factor in LEO; it is the most significant cause of deterioration of many spacecraft materials, such as polymers and optical coatings.[1,2,10,11] There are other environmental effects, such as charging (electrostatic discharge effects) and thermal cycles, typically between −100 and 100 °C. Charging of the spacecraft external surfaces is especially critical in GEO, where communication satellites typically operate.[1]

AO forms as a result of UV-induced dissociation of molecular oxygen. AO is most abundant in LEO and is harmful to the satellite exteriors due to oxidation and erosion.[1,12] While the oxygen atoms are thermal and of low density ($\approx 10^8$ cm^{-3}), their collisions with the exteriors of space vehicles that orbit at a velocity of 8 km s^{-1} are equivalent to an impact energy of $\approx$4.5–5 eV and a flux of 10^{14}–10^{15} O-atoms cm^{-2} s^{-1}. The AO flux is influenced by the altitude, the solar activity variation, the orbital inclination, and the time of year; therefore, it is particularly challenging to predict the AO flux.

The increased human space activity has created numerous hypervelocity objects, namely space debris. The amount of space debris is steadily increasing over time; nowadays we can account for more than 18 000 large (10 cm and above) objects and uncounted number of smaller ones.[13] These, along with

Dr. I. Gouzman, Dr. E. Grossman, Dr. R. Verker, Dr. N. Atar, Dr. A. Bolker
Space Environment Department
Soreq Nuclear Research Center (NRC)
Yavne 81800, Israel
Prof. N. Eliaz
Department of Materials Science and Engineering
Tel-Aviv University
Ramat Aviv, Tel-Aviv 6997801, Israel
E-mail: neliaz@tau.ac.il

The ORCID identification number(s) for the author(s) of this article can be found under https://doi.org/10.1002/adma.201807738.

naturally existing ultrahigh-velocity meteoroids, pose a substantial threat to spacecraft. The collision velocities of space debris vary between 3 and 15 km s^{-1}, with an average of $\approx$10 km s^{-1}.[14] Collisions with space debris or meteoroids might end in damage or complete failure of external units, such as solar cells, affect the properties and performance of materials, contaminate optical devices, or even destroy satellites. Such collisions typically result in formation of new debris, thus increasing the risk to future missions.

The space environment affects all materials and systems of the satellite; however, external components, including thermal blankets, thermal control coatings, and optical sensors, are most affected by its individual constituents and their synergistic effects. Thus, the key for the development of novel materials for space applications is thorough ground durability testing in order to avoid failures in the real space environment.

This progress report describes mainly polyimide (PI) modifications to withstand the effects of AO and electrical charging, as well as the use of novel technologies to produce novel PI-based materials and their 3D structures for space applications. These include conductive composite materials based on PI infiltration into carbon nanotube (CNT) sheets or 3D-graphene structures; hybrid self-passivating PIs; thermoformed 3D PI structures; and 3D printing of PIs, including our groundbreaking results on 3D printing by the PolyJet technology.

2. Polyimides

Polyimides are very promising engineering polymers, exhibiting high-temperature resistance, low-temperature tolerance, outstanding mechanical properties, chemical and radiation resistance, flexibility, and excellent dielectric properties. The reputation of PIs has been established on the basis of exceptional properties and versatility unparalleled by most other classes of macromolecules. There are both thermosetting and thermoplastic PIs. PI synthesis routes include polycondensation or addition mechanisms. The number of PI monomer precursors is huge; the structure-property relationship is in many cases not fully predictable, and the range of applications is enormous. There are many published comprehensive works on PIs' chemistry, synthesis, characterization, and applications.[15–24] Since the first synthesis of PIs pioneered by chemists at Dupont in the 1950s, and to this day, they have turned into real high-performance materials for use in advanced engineering applications, particularly in the microelectronics and aerospace industries. Space applications use most often aromatic PIs. Kapton is prepared through condensation polymerization of pyromellitic dianhydride (PMDA) and oxydianiline (ODA) (see inset (a) in **Figure 1**). It is commonly used as thermal blankets, i.e., the external layers in a multilayer insulator (MLI) structure, that insulate satellites from the solar radiation.[22] Flexible solar arrays, matrix resin for composites, coatings, and high-temperature adhesives are just a few examples of common PI applications.[15,16,22,24]

The development of PI-based shape memory polymers (SMPs) for space applications is currently of great interest.[25–28] Such applications include large-area flexible electronics, deployable structures and devices for use in a lunar base, deployable

Irina Gouzman received her Ph.D. degree in physical chemistry in 1999 from the Technion-Israel Institute of Technology. Her research interests are in the areas of applied surface science, nanodiamond films deposition, and materials characterization by a variety of electron spectroscopy techniques. In 2004–2005, she spent her sabbatical at the Department of Chemistry at Princeton University, focusing on high-resolution X-ray photoelectron spectroscopy studies of interface chemistry, mainly in the field of self-assembled monolayers of organic films on electronic materials. Currently, she is the head of the Space Environment Department at Soreq NRC and a board member of the Israel Vacuum Society.

Eitan Grossman received his Ph.D. degree in materials engineering in 1986 from Ben-Gurion University in Beer-Sheva, Israel. His research interests include interaction of space environment components, such as atomic oxygen, hypervelocity debris impact, and ultraviolet and ionizing radiation, with materials. He specializes in polymers and surface analysis techniques, with emphasis on scanning probe microscopy. In 2005—2006, he spent a sabbatical year at the University of Chicago, studying photochemical reactions and gas transport mechanism in polymers. After heading the Space Environment Department for several years, he currently holds the position of Deputy of the Technology Division at Soreq NRC.

solar batteries, solar sails, and sun shields for the next generation of space telescopes. SMPs and shape memory polymer-based composites (SMPCs) are smart materials that can be converted into a temporary shape and then restored to the original shape under an external stimulus such as heat, electromagnetic or electrical fields, light, and chemical vapors or liquids. The shape memory effect (SME) of SMPs is usually explained by a dual-phase mechanism: a permanent phase that consists of the nodes of macromolecule segments related to physical or chemical crosslinks, and a reversible phase that consists of the molecular chains. In order to avoid inadvertent triggering, the glass-transition temperature, T_g, of the SMP should be higher than the ambient temperature. Hence, shape memory PIs with different T_g values are needed for different environments and temperatures. For thermoplastic shape memory PI, the reversible phase originates from the aromatic
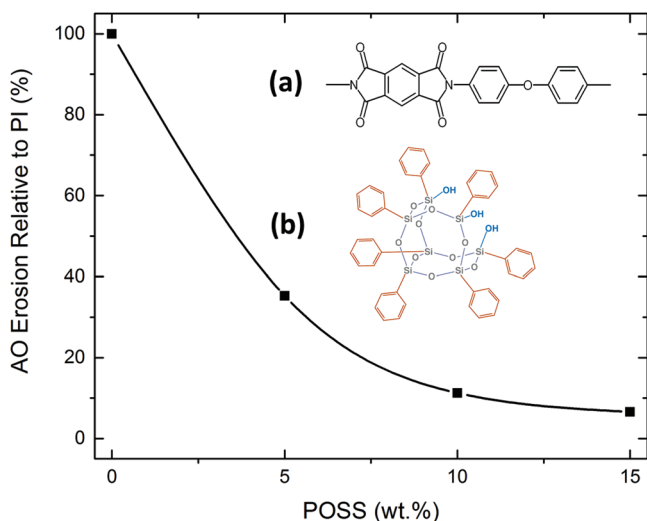
Figure 1. The dependence of AO erosion of POSS-PI samples on the POSS concentration. Inset: Schematics of a) PI monomer and b) TSP–POSS molecule. Reproduced with permission.[48] Copyright 2011, Tel-Aviv University.

Noam Eliaz is a full professor, founder of the Department of Materials Science and Engineering, founding director of the Tel-Aviv University (TAU) new AM R&D Center, and a member of The Israel Young Academy. He received his B.Sc. and Ph.D. degrees (direct track) in materials engineering and M.B.A., all *cum laude*, from Ben-Gurion University. In the Academic Reserve, he served as a Metallurgical Laboratory Officer at the Israel Air Force. Prior to joining TAU in 2001, he was a Fulbright and Rothschild Fellow at MIT. His research interests include additive manufacturing, biomaterials, bioferrography, electrodeposition, corrosion, failure analysis, and materials for space applications.

chains with flexible elements in the backbone, while the fixed phase is based on the high-molecular-weight chains forming the physical crosslinks. Thermoset shape memory PIs have higher T_g and storage moduli and better shape fixity compared to their thermoplastic counterparts due to their low-density covalent crosslinking.[27] Shape memory composites (SMCs) can be formed by either using SMP matrices or by integrating parts made of SMPs. Flexible composite skins over a shape memory foam core can be used to obtain a composite sandwich that can be shaped to reduce its volume or to change its stiffness.[29]

3. Modification of Polyimides for Survivability in LEO

One of the major design concerns for the external satellite materials in LEO is protection against AO erosion.[30,31] PIs, like other hydrocarbon-based polymers, are very sensitive to AO attack and require protective coating. For example, PI surfaces coated with SiO_2 show AO erosion yield lower than 1% of those of bare PI. Tagawa et al.[32] evaluated the minimal thickness of amorphous α-SiO_2 protective coating required to avoid bulk diffusion of AO in LEO by measuring the thickness of the oxide layer formed on Si(001) wafers under a hyperthermal AO beam. A few nanometers thick coating was found efficient. The diffusion length of AO in α-SiO_2 increased as the temperature was raised within the tested range of 24 to 220 °C, as well as with increasing beam flux. These findings suggest that a thicker coating is required to prevent AO diffusion in LEO, where high AO flux exists. However, defects in the protective coating, either inherent or produced by hypervelocity impacts, will result in oxygen penetration and will permit accelerated AO erosion of the underlying polymer, a phenomenon known as undercutting.[33,34] AO undercutting of protected Kapton has been extensively studied, both experimentally and
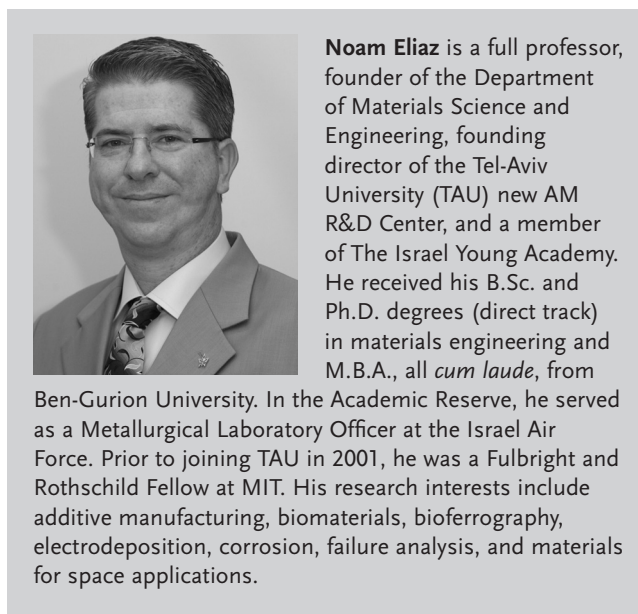
theoretically.[35,36] Various protective coatings have been developed, with emphasis on their electrical properties. For example, indium tin oxide (ITO) is used in applications where electrostatic discharge (ESD) protection is essential.[37] We have applied TiO_2 and SnO_2 coatings on Kapton films by the liquid phase deposition (LPD) process.[38–40] Minton et al.[41] studied the efficacy of atomic layer deposited (ALD) Al_2O_3 and TiO_2 coatings in protecting Kapton H, FEP Teflon, and poly(methyl methacrylate) (PMMA) films from AO and VUV attack. While the alumina ALD coatings protected the underlying substrates from AO attack, titania coatings also protected the substrates from VUV-induced damage. Man et al.[42] modified the surface of Kapton by low-concentration $NH_3 \cdot H_2O$ and silicon coupling agent to improve the polymer surface wettability. Consequently, the adhesion between the Kapton substrate and TiO_2/SiO_2 multilayer coatings prepared by a sol–gel process was improved. Unfortunately, all ceramic coatings could be damaged and cracked by either handling on Earth or thermal cycling, as well as by micrometeoroid and debris impacts in space, thus leaving the underlying material subjected to AO attack.[43]

An alternative favorable approach for fabrication of LEO-durable polymers is the development of advanced hybrid materials that possess *self-passivating* ability in an oxidative environment. This can be done by incorporation of polyhedral oligomeric silsesquioxane (POSS) into the polymeric chains, forming organic–inorganic hybrid copolymers and blends.[43–51] Incorporation of POSS into PI films has significantly decreased the erosion yield of PI due to formation of SiO_2 passivation layer. The SiO_2 passivation layer formed by surface interaction with AO prevents further erosion of the polymer (see Figure 1). This means that AO erosion through inherent or space debris impact-induced defects will be prevented by self-passivation.

We have studied the effects of simulated hypervelocity debris and AO on PI and POSS–PI nanocomposite films. Kapton HN films were exposed to aluminum flyers with impact velocities as high as 2.9 km s^{-1} using a laser-driven flyer (LDF) ground

**ADVANCED
SCIENCE NEWS**

www.advancedsciencenews.com

**ADVANCED
MATERIALS**

www.advmat.de

simulation facility.[52] Fractography showed a change in the film fracture mode from brittle to ductile when the Kapton film thickness was increased from 25 to 125 µm. The increase in flyers' velocity has a similar effect, namely a transition from ductile to brittle fracture. Impacts at velocities higher than 1.7 km s^{-1} exhibited a mixed fracture mode: the central impact regions were characterized by ductile-type fracture due to higher strain rate, while the outer regions were characterized by brittle cracking since they were subjected to a lower strain rate. A model was suggested to explain this behavior based on the developed impact temperature relative to the film's T_g. It should be noted that the exposure of PI films to hypervelocity impacts by other types of flyers, e.g., SiO$_2$ microparticles originating from silicone contaminants outgassed from silicone adhesive and AO irradiated to form these SiO$_2$ microparticles,[53] should also be studied.

Next, we studied individual and synergistic effects of ultrahigh-velocity impacts and AO on PMDA–ODA PI films.[54] Following hypervelocity impact and subsequent exposure to oxygen RF plasma, which simulates AO in space, a synergistic erosion effect was observed. The accelerated degradation of the PI was manifested mainly by the formation of new AO-induced macro-holes. These holes were observed in a radial star-like pattern around the initial impact zone. This phenomenon was explained by the formation of residual tensile stresses around the impacted area. The residual stresses, in turn, generate a local increase in the polymer's free volume. The latter could enhance oxygen diffusion into the polymer, which accelerates the localized high-rate degradation of the material. We also studied the combined effect of simulated hypervelocity debris impact and AO exposure on the degradation of blends of trisilanolphenyl (TSP)–POSS and PMDA–ODA PI.[55] The POSS (15 wt%)–PI films were more resistant to both debris impact and AO exposure after impact. This durability was attributed to a combination of low residual tensile stresses and formation of an oxide passivation layer.[55,56] The POSS content affects the mechanical properties and the fracture mechanism of POSS–PI nanocomposites.[47] The formation of POSS aggregates was found to be the main factor that influences the nanocomposite mechanical properties. POSS aggregates were created by either physical phase separation or chemical POSS–POSS condensation reaction. A correlation between the POSS aggregate parameters and the mechanical properties of the nanocomposite was established. We suggested a model describing formation and coalescence of voids during tensile tests in order to understand the influence of the POSS content on the POSS–PI mechanical response.[47] It was shown that POSS–PI typically exhibits higher susceptibility to hypervelocity impact than pure PI under extreme temperature conditions (between −60 and 100 °C). This was evident by the formation of a larger perforation area through film shearing, as well as aggregate debonding and voids coalescence during hypervelocity impact. Vulnerability of the POSS–PI film to shearing at low temperatures (−60 °C) was explained by the lower degree of chain mobility and higher stress concentrations that developed at the POSS-aggregates' debonded sites. The shearing effect of the POSS–PI film at high temperatures (100 °C) during hypervelocity impact was attributed to the higher chain mobility, which allows a faster coalescence of the voids that had formed at debonding

sites. Void coalescence accelerates film shearing by hypervelocity impact.[46] Void coalescence may also be facilitated by a decrease in T_g as POSS loading is increased, possibly due to a plasticization effect of the POSS molecules.[57]

POSS–PI copolymers have demonstrated excellent durability to hyperthermal AO attack as proven by both laboratory tests and *in-flight* exposures within the materials interactions space station experiments (MISSE) conducted onboard the International Space Station (ISS). Minton et al.[51] have compared the erosion yield of blends of POSS monomers with a PI to the erosion yield of POSS–PI copolymers. It was found that the main factor affecting the erosion yield of the POSS–PI materials is mainly the wt% of the silicon–oxygen cage, while the chemical nature of the POSS monomer bonding to the polymer backbone, i.e., chemically copolymerized or grafted, or physically blended, has a minor effect. Comparison of the erosion results obtained by ground hyperthermal AO beam tests to those obtained from space flight and at similar AO fluences indicates that the hyperthermal AO beam exposure faithfully simulates the AO effects observed in LEO environment.[43] POSS–PI copolymers with a POSS cage content of as high as 7 wt% revealed an excellent AO resistance with no adverse effects on either the thermal or mechanical properties. Therefore, POSS–PI can be recommended as an ideal alternative for Kapton on the spacecraft exteriors in LEO. It has also been suggested to incorporate both POSS and phosphorous into the main chain of the PI.[58] This phosphorous addition resulted in both increase of T_g and enhanced thermal stability. Song et al. reported that the AO erosion yield was reduced to 51.9% of that of 3.17 wt% POSS–PI nanocomposites when the phosphorus concentration was 1.61 wt%. This was related to the presence of phosphorus-containing bis(4-aminophenoxy)phenyl phosphine oxide (DAPPO) monomer in the phosphorus-containing PI–POSS hybrid, and the formation of a passivating phosphate and metaphosphate surface layer after AO exposure.[58]

Photocurable silsesquioxanes (RSiO$_{1.5}$) are a new type of organic–inorganic hybrid materials that consist of photoinitiated polymerizable groups (organic components) incorporated in silsesquioxane frameworks (inorganic components) as multifunctional groups at the intramolecular level. Photocurable silsesquioxane coatings on PI films have been developed. They were applied using the roll-to-roll wet-coating technology and showed excellent resistance to AO, electron beam, and UV irradiations, thermal cycles, and high-temperature vacuum conditions.[59] Hybrid POSS-containing coatings have also been suggested, including polysiloxane/POSS hybrid coatings on Kapton.[60] The AO erosion yield of the coated Kapton was 2 orders of magnitude lower than that of pristine Kapton. Another approach was suggested by Zhang and co-workers,[61,62] who prepared a space-survivable PI with outstanding thermal stability, high optical transparency, decent mechanical strength, suitable elongation to fracture, and exceptional AO erosion resistance by first synthesizing hyperbranched polysiloxane (HBPSi), and then incorporating HBPSi into PI chains via copolycondensation reactions. During exposure of HBPSi PI to AO, the organic PI at the surface was first degraded, and a silica protective film ultimately formed, thus enabling the surface to "self-heal." A percolation threshold of HBPSi addition to attain the appropriate AO durability upon

**ADVANCED
SCIENCE NEWS**

www.advancedsciencenews.com

**ADVANCED
MATERIALS**

www.advmat.de

AO exposure was observed and was attributed to the quick formation of a dense silica passivation layer on the surface at high HBPSi content. The same group later studied the AO durability of eight Si-containing PI thin films.[63] These films showed high thermal stability and better AO resistance, but also a somewhat inferior mechanical performance compared to pristine PI. It was shown that Si-containing units with higher oxidation states and higher Si/O atomic ratio were better in improving the AO resistance. In some cases, the oxidation state of Si had a more profound effect on the AO resistance than the Si concentration. Qi and Zhang[64] prepared a series of PI/SiO_2 hybrid foams by the sol–gel process. Aminopropyl-triethoxysilane (APTEOS) was used as the coupling agent to improve the compatibility between the PI matrix and SiO_2. The hydrogen bonding between the PI matrix and the SiO_2 limited the molecular mobility and improved their interfacial adhesion. The thermal stability, storage modulus, glass-transition temperature, and dielectric constant of the hybrid foams were enhanced by incorporation of SiO_2. The AO erosion performance of the hybrid foams was also enhanced due to the formation of a SiO_2 protective layer on the surface of these foams following AO exposure.

Reactive molecular dynamics (MD) simulation has been used to investigate the initial effects of AO irradiation on PI, POSS, POSS-PI, amorphous silica, Teflon, graphene, and CNTs in a PI matrix.[65,66] The role of impact energy, the composition of the material, and its temperature were also evaluated. It was found that a decrease in the local temperature evolution in materials during AO irradiation can increase the material stability.[65] Rahmani et al. claim that the normalized mass loss, surface damage, and AO penetration depth are affected by the PI composite fillers concentration and orientation.[66] PI systems with randomly oriented CNTs and graphene were found to be more stable compared to those with aligned CNTs and graphene at the same nanoparticle concentration. This difference was attributed to the amount of exposed PI on the material surface in each case. Other types of nanofillers theoretically studied were pristine POSS and PI-grafted POSS. It was found that grafting the POSS and increasing the POSS concentration from 15 to 30 wt% resulted in a better AO durability, by a factor of about 4 and 1.5, respectively. The increase in durability is explained by a better dispersion of PI-grafted POSS in the PI matrix compared to that of the pristine POSS.[66]

4. Polyimide–Carbon Nanocomposites

Recent advances in the development of nanomaterials with exceptional mechanical properties, such as CNTs and 2D- and 3D-graphene, have led to substantial attempts to use them as reinforcements in polymer matrices.[67,68] Besides excellent mechanical properties, these materials provide electrical conductivity, which is required in order to prevent ESD in polar LEO and GEO orbits.

PI films are electrically insulating, thereby enabling charge accumulation and eventually ESD, which introduces a threat for spacecraft electronics under exposure to space plasma. One of the novel approaches to attain ESD protection of PI films is to incorporate electrically conducting additives, such as CNTs[69–71] or graphene, into the PI matrix.

4.1. Carbon Nanotubes

Although CNTs were introduced over two decades ago, their application in space missions remains a challenge. CNT potential for space systems and the technological gap that must be overcome for their application have been recently reviewed.[68] CNTs have been used for ESD protection in the form of an electrically conductive CNT-based sheet material (rather than as additive material) incorporated into NASA's Juno spacecraft.[72,73]

Compared to other conductive additives, CNTs have key advantages thanks to their enormously high aspect ratio and high conductivity, which allow using lower additive concentrations. Common incorporation methods are based on dispersion of CNT powder in polymer matrices by means of sonication[69–71,74–77] and functionalization[69,76,77] to improve homogeneity. However, these incorporation procedures frequently end in significant degradation of the CNTs' electrical, thermal, and mechanical properties.[78] Additionally, due to the strong van der Waals forces, CNTs tend to agglomerate into bundles in the polymer matrix. Improving the electrical conductivity of the composite material by increasing the CNT content is also problematic because the formation of homogeneous dispersions and the removal of large volumes of solvents are not easy. Consequently, the mechanical properties of the final composite are often degraded.[79,80]

Recently, electrically conductive and highly aligned multiwall CNT (MWCNT)–PI nanofibrous composites were fabricated using the electrospinning technique and incorporating poly(ethylene oxide) as the dispersing medium.[81] Functionalized 3 and 9 vol% MWCNTs were uniformly dispersed on the surface of PI nanofibers, as shown in **Figure 2**a. Liao et al. fabricated PI nanocomposites with CNTs and graphene oxide as fillers by in situ polymerization.[82] Figure 2b presents an SEM image of the lamellar structures in the cross-section of the composite film, where no obvious agglomeration of the CNTs and graphene is observed. This is due to the solvent-exchange method that facilitated the uniform distribution of CNTs with graphene oxide in the PI matrix.

Recently, new methods have been developed to enable control over the CNT dispersion within polymer matrices without damaging the CNT structure. One of the promising techniques uses polymer solution infiltration into CNT sheets grown by chemical vapor deposition (CVD).[83–87] Using this method, agglomeration is prevented since the CNTs are fixed to a substrate and, hence, their location and orientation are inherently preserved. The infiltration method is effective in producing CNT composites with high loading levels[88,89] and avoiding residues of solvents or surfactants. Furthermore, by prepatterning the catalyst on the substrate, it is possible to grow CNTs with desired architectures.[83,90,91]

In our recent studies, conductive CNT–PI composite films were prepared by infiltration of polyamic acid into entangled CNT sheets that were grown by CVD.[92] The role of the PI matrix is to enhance the mechanical stability and provide

ADVANCED
SCIENCE NEWS
www.advancedsciencenews.com

ADVANCED
MATERIALS
www.advmat.de
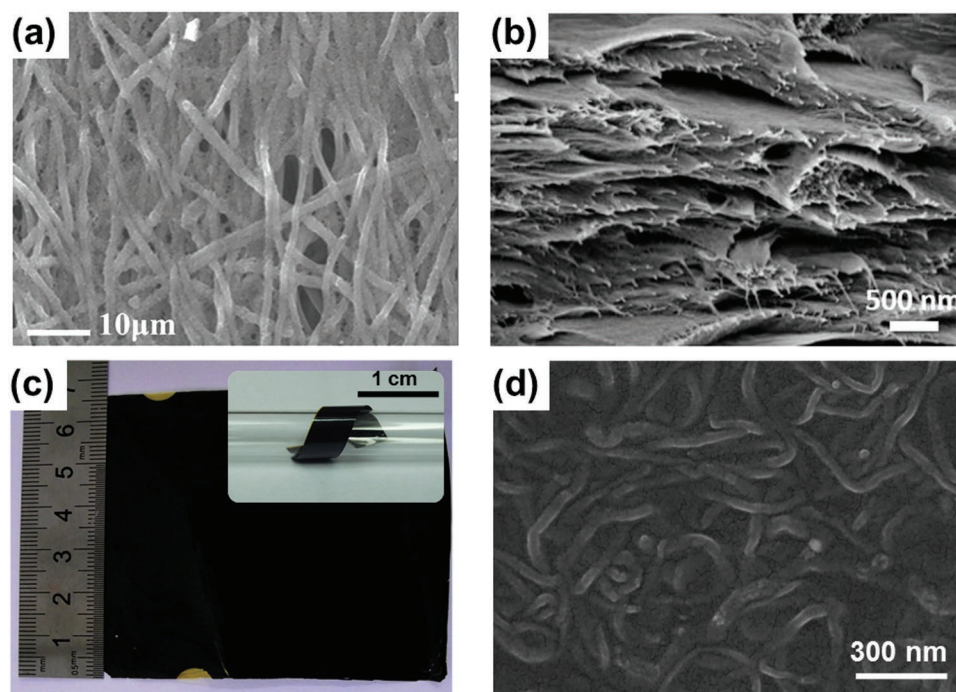
Figure 2. a) SEM image of the surface of PI nanofibrous composite with 3 vol% MWCNTs. Reproduced with permission.[81] Copyright 2014, AIP Publishing. b) SEM image of the cross-section of CNT–graphene oxide–PI nanocomposite. Reproduced with permission.[82] Copyright 2017, Elsevier. c) Optical image of a CNT–POSS–PI film. Inset: Flexible freestanding CNT–POSS–PI film wrapped around a 2.9 mm diameter glass tube. Reproduced with permission.[93] Copyright 2015, American Chemical Society. d) HRSEM image of the CNT–POSS–PI film surface. Reproduced with permission.[93] Copyright 2015, American Chemical Society.

robustness and flexibility to the composite film. The CNT structure that provides the electrical conductivity was used in the as-grown sheet configuration, without any additional treatments for improvement of wettability or homogeneity. The resulting CNT–PI composites possess high isotropic electrical conductivity and good anticipated durability in GEO environment. However, they are expected to erode when exposed to AO in LEO. Therefore, in order to reduce the erosion of the CNT–PI composites, POSS–PI replaced the pure PI, resulting in highly AO-resistant CNT–POSS–PI films.[93]

Two representative macroscopic images of CNT–POSS–PI freestanding films are displayed in Figure 2c. The flexibility of the freestanding composite films is demonstrated in the inset, which shows the CNT–POSS–PI film wrapped around a 2.9 mm diameter glass tube. The typical surface morphology of a CNT–POSS–PI film observed by high-resolution scanning electron microscope (HRSEM) is presented in Figure 2d, demonstrating homogeneously distributed CNTs in the PI-based matrix.

4.2. Graphene

Another proposed conductive additive is based on novel 2D material, e.g., graphene. 3D foam-like materials have been suggested recently as a new means of transforming 2D graphene into 3D shapes.[94] These 3D porous materials preserve many of the unique properties of their constituent 2D material, while establishing a bulky, flexible, ultralight 3D network.

3D-graphene (denoted as 3D-C) has an interconnected structure that consists of multilayer graphene.[95,96] It was found as a filler that effectively improves the electrical and thermal characteristics of polymers. 3D-C has the benefits of high specific surface area, high mechanical strength, and excellent thermal[97,98] and electrical[94] transport kinetics. Its possible applications include stretchable electronics,[94,99] energy storage,[100] and chemical and mechanical sensing.[101,102] Jia et al.[103] demonstrated the effectiveness of 3D-C as a filler material in epoxy, increasing the composite conductivity by 12 orders of magnitude, to 3 S cm^{-1}. This was achieved by using a 3D-C structure containing roughly four graphene layers, which is equivalent to 0.1 wt% filler content. Meng et al.[104] have shown the use of an interconnected PI-supported 3D graphene structure as a basis for flexible electrodes for lithium-ion batteries. Recently, Yoonessi et al.[105] produced a graphene–PI nanocomposite containing well-dispersed graphene nanosheets. The maximum conductivity achieved was 0.96 S cm^{-1} at a filler content of 5 vol%. This value is three times lower than the conductivity achieved using 3D-C with similar and lower loading fractions.[103,106] Therefore, the 3D-C interconnected graphene structure presents several advantages over other conductive nanofillers such as CNTs, metallic nanoparticles, and graphene flakes. Thanks to the interconnected structure, there is no need to increase the filler fraction in order to pass a percolation limit to reach high electrical and thermal conductivities. In addition, traditional powder nanofillers tend to have inhomogeneous distribution, aggregation, and limited filler fraction due to their effect on the structural integrity of the polymer matrix. Fillers incorporation

1807738 (6 of 15)

Table 1. Comparison of the thermal conductivity of various reported filler–PI composite films.[106]

	Filling factor		Thermal conductivity [W m^{-1} K^{-1}]		Normalized increase per 0.1% filling factor		Ref.
	[wt%]	[vol%]	Bare PI	Filled PI	[wt%]	[vol%]	
SiC nanowires on graphene	7		0.25	0.577	0.0047		[109]
	11		0.25	2.63	0.022		[110]
MWCNTs	3		0.18	0.25	0.0023		[111]
BN–c-MWCNTs	3		0.18	0.38	0.0067		[111]
Silver particles		45	0.2	15		0.033	[114]
BN	30		0.18	1.2	0.0034		[113]
Aluminum nitride nanoparticles		30	0.22	0.6		0.0013	[115]
		10	0.26	0.32		0.0006	[112]
3D-C	0.35	0.3	0.15	1.7	0.443	0.5167	[106]

might lead to different effects, including bending, curling, cracking, displacement, and delamination.[107,108]

In our recent studies, highly conductive 3D-C/PI (i.e., 3D graphene with PI) composite films were developed.[106] This composite demonstrated stable long-term reliability in ground-based simulated space environment tests. Its electrical and thermal properties, as well as aging effect under various bending and thermal cycles, were also investigated. 3D-C-infused PI films were found to retain the excellent electrical and thermal conductivity of the 3D-C. This material passed the space environment qualification tests; thus, it can be used as an ESD shielding protection with proven long-term stability.[106] The incorporation of 3D-C in PI matrix improves the PIs' electrical and thermal conductivities by up to 10 orders of magnitude, to roughly 3.5 Ω □$^{-1}$ and 1.7 W m^{-1} K^{-1}, respectively. The thermal conductivity of PI with various fillers is shown in **Table 1** in comparison to the thermal conductivity of 3D-C/PI.[106] The fillers include graphene,[109,110] CNTs,[111] and metal particles.[112–115]

The images in **Figure 3** show different graphene–PI composites. Figure 3a displays a bare 3D-C foam and a homogeneously distributed PI along the 3D-C matrix achieved in our recent work.[106] Figure 3b shows HRSEM cross-section images of both bare and PI-infiltrated 3D-C. It is evident that the entire highly porous structure of 3D-C has been completely filled with PI.[106] Figure 3c shows a scanning tunneling microscopy (STM) image at atomic resolution of the 3D-C with a hexagonal symmetry modulation of 0.246 nm periodicity.[106] Figure 3d shows an SEM image depicting the interconnected macroporous structure of the 3D-C/PI electrode produced by Meng et al.[104] Figure 3e shows a low-magnification transmission electron microscope (TEM) image revealing the dispersion of the graphene layers and stacks in the nanocomposite produced by Yoonessi et al.,[105] with graphene concentration of 1.23 vol%. Both high particle number density of the graphene layers and stacks were evident.

4.3. Space Durability of Polyimide–Carbon Nanocomposites

The space durability of the aforementioned PI–carbon nanocomposites was investigated, focusing on the AO erosion and electrical conductivity for ESD prevention, as described below.

Yuan et al.[69] reported preparation of solution-casted PI nanocomposites with a maximal MWCNT content of 30 wt%, and improved electrical and mechanical properties. As shown in **Figure 4**a, the electrical conductivity of the MWCNT–PI composites reaches a value of 38.8 S cm^{-1} at nanotube concentration of 30 wt%; the MWCNT content for attaining the composite's conductivity percolation threshold is 0.48 wt%. These are, correspondingly, the highest and among the lowest values reported for any conventional solution-processed nanotube composite.

The conductivity of the graphene nanosheet–PI composite produced by Yoonessi et al.[105] is shown in Figure 4b as a function of the graphene volume fraction. The results indicate that the percolation transition to a conducting nanocomposite occurs at a graphene concentration of 0.03 vol%, and that the maximal conductivity (0.94 S cm^{-1}) is attained at higher graphene concentration (5 vol%). This value is three times lower than the conductivity achieved using our 3D-C/PI and 3D-C/epoxy with either similar or lower loading fractions.[103,106]

Our recent works reported the sheet resistance of various PI nanocomposites with different fillers—3D graphene, CNT, and POSS (5 and 15 wt%)—as a function of temperature.[93,106] The results obtained using a four-point Hall/resistivity system and the van der Pauw method indicate that the PI-based nanocomposites well satisfy the antistatic criterion, which is essential in space applications.[116] Figure 4c shows that the sheet resistance of the CNT–POSS–PI films is roughly 200 Ω □$^{-1}$ at room temperature (RT), about 25% higher compared to a pristine CNT film, and one order of magnitude higher than other CNT-PI composites presented in Figure 4a (14 wt%, 13.3 S cm^{-1}). Figure 4c also shows that the sheet resistance of the 3D-C/PI films is roughly 4 Ω □$^{-1}$, 2 orders of magnitude lower than that of CNT–POSS–PI films, but still 12.5% higher compared to the pristine 3D-C foam. Moreover, the PI infiltration into the CNT or 3D-C did not cause any parasitic effect on their intrinsic electrical conductivity. The electrical conductivity mechanism of both CNT–PI and 3D-C/PI films was reported to best fit the variable range hopping (VRH) model by Godet (see Figure 4d)[117–119]

$$\sigma(T) = \sigma^{00} T^{-1/2} \exp\left(-\left(T_0/T\right)^{1/4}\right) \quad (1)$$

where σ^{00} is a constant, $T_0^{1/4}$ is the slope of the trend line of an Arrhenius curve of $\ln(\sigma T^{1/2})$ versus $T^{-1/4}$ (shown in Figure 4d),
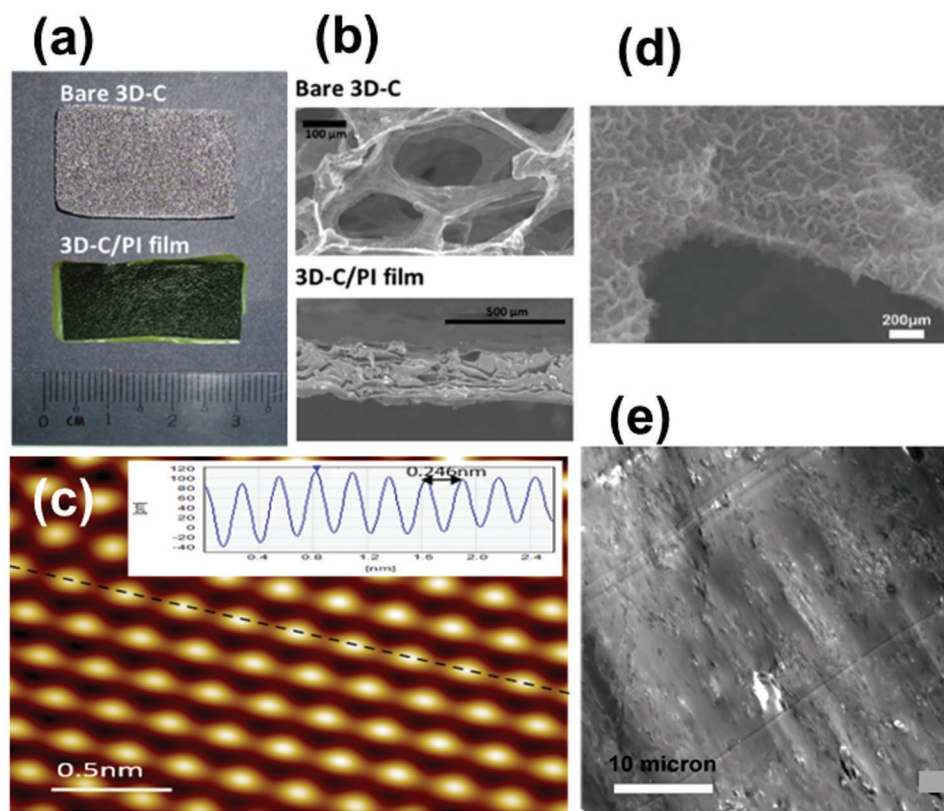
Figure 3. Microscopic images of graphene–PI composites. a) Optical image of the bare 3D-C and the nanocomposite film. Reproduced with permission.[106] Copyright 2015, Wiley-VCH. b) HRSEM cross-section images of bare 3D-C and 3D-C/PI film. Reproduced with permission.[106] Copyright 2015, Wiley-VCH. c) Inverse fast Fourier transform (FFT) of an STM atomic-resolution image of the 3D-C, showing the triangle lattice characteristic of the coupling between the upper graphene layer and the layer beneath (30 mV, 2 nA). Inset: A line scan (indicated as a black dotted line in the main figure) shows a distance of 0.246 nm between each individual atom. Reproduced with permission.[106] Copyright 2015, Wiley-VCH. d) SEM image of a 3D reduced graphene oxide (RGO)/PI cross-section. Vertically aligned PI nanoflakes are observed on the 3D-RGO. Reproduced with permission.[104] Copyright 2014, Royal Society of Chemistry. e) TEM image of a graphene–PI nanocomposite, showing the local dispersion of the graphene nanosheets and expanded graphene clusters and fractal. Reproduced with permission.[105] Copyright 2017, American Chemical Society.

and σ is associated with sample conductivity (S cm^{-1}). σ was calculated as the inverse value of the multiplication of the sheet resistivity and the thickness.

As mentioned above, carbon-based materials might be eroded when exposed to AO, the dominant species at LEO altitudes. Rahmani et al.[66] found that a PI system reinforced with randomly oriented CNT or graphene nanoparticles exhibits a higher resistance to AO compared to some other systems. For example, the theoretically simulated normalized mass loss (mass loss was normalized with respect to the initial total mass at t_0) as a function of fluence is shown in **Figure 5**a for pristine PI and PI systems loaded with POSS, as well as randomly oriented and aligned graphene and CNT nanoparticles with a concentration of 15 wt%.

Novikov et al.[120] reported results of ground-based simulation of AO influence on samples of PI composites with different fillers (polyorganosiloxanes, MWCNTs, detonation nanodiamonds (DNDs), and inorganic nanoparticles of Al$_2$O$_3$, TiO$_2$, and WC). Two types of polyorganosiloxanes were used. The first one is a hyperbranched polyetoxysiloxane (HPES), a globular structure with a high content of ethoxy groups (–OC$_2$H$_5$) capable of subsequent transformations. This

structure is virtually free of cyclic fragments. The second one, amorphous silica sol (SS), is a high-temperature hydrolysis product of HPES. The calculated mass erosion yields R_e for PI samples with different fillers (3 wt% content) exposed to AO fluence of 6.0×10^{20} atom cm^{-2} were $\approx 2 \times 10^{-24}$ g O-atom^{-1} for the polyorganosiloxanes and $\approx 3.5 \times 10^{-24}$ g O-atom^{-1} for the inorganic particles. Polyetoxysiloxanes as fillers in PI composites provided lower mass erosion yield in comparison with inorganic particles. One can argue that these results are the outcome of the tendency of inorganic nanoparticles to agglomerate due to van der Waals forces instead of chemical bonding (as for polyetoxysiloxanes). The graph in Figure 5b presents calculations of the reduction in mass erosion yield for PI composites with pristine MWCNTs (PI-CNT1), functionalized MWCNTs (PI-CNT2), and DNDs as fillers. Smaller values of mass erosion yield were obtained with functionalized CNTs in comparison with pristine CNTs and DNDs due to their stronger interaction with polymer chains, which led to a better dispersion in the polymeric matrix. Additionally, it can be seen that reduction of the erosion yield for most samples was ≈ 10–20%, which is relatively small in comparison with polyorganosiloxanes.
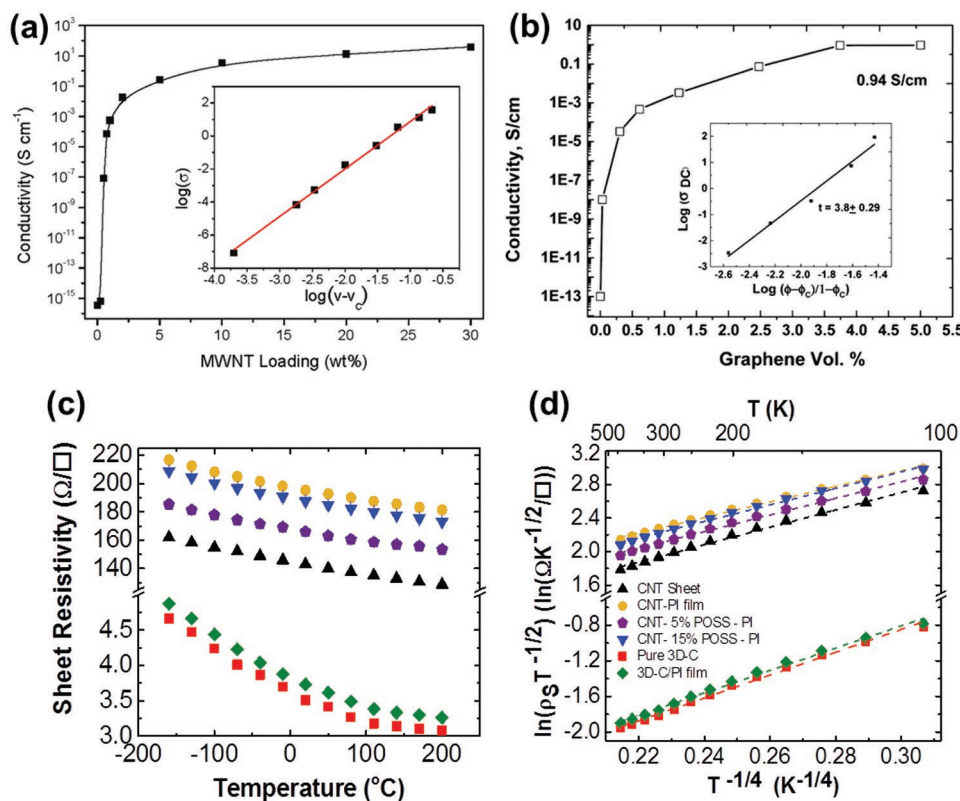
Figure 4. Electrical characterization of PI-based nanocomposite films. a) Log DC conductivity for MWCNT–PI composites, measured at room temperature, as a function of the MWCNT mass fraction. The inset shows the fit to the conductivity data for determination of the percolation threshold. Reproduced with permission.[69] Copyright 2011, American Chemical Society. b) DC conductivity of the PI–graphene nanocomposites. The inset shows fit of the data to the power law predicted by the percolation theory. Reproduced with permission.[105] Copyright 2017, American Chemical Society. c) Sheet resistance of bare 3D-C, 3D-C/PI, pristine CNT sheet, and CNT–POSS–PI films (0, 5, and 15 wt% POSS content) at a temperature range of −160 to 200 °C.[93,106] Legend is given in (d). Reproduced with permission.[106] Copyright 2015, Wiley-VCH. d) Fit of the data in (c) to the VRH model.[93,106] Reproduced with permission.[106] Copyright 2015, Wiley-VCH.

We reported a ground-based AO exposure of CNT–POSS–PI films (0, 5, and 15 wt% POSS) to different AO fluences, in the range of 6.0×10^{19} to 2.9×10^{20} O-atoms cm^{-2}.[93] The erosion yield of the CNT–POSS–PI films was determined as a function of AO fluence (Figure 5c), and was compared to the accepted erosion yield of Kapton H.[121] The erosion yield of CNT–PI films was found to be 4.7×10^{-24} cm^3 atom^{-1} (56% higher than the erosion yield of Kapton H), and was not affected by change in the AO fluence. The erosion yield of CNT–POSS–PI films decreased drastically with increase of the AO fluence due to O atom–induced formation of a passivation layer. The ultimate erosion yield of the CNT–POSS–PI films with 5 and 15 wt% POSS content was estimated as 1.3×10^{-24} and 3.1×10^{-25} cm^3 atom^{-1} (43% and 10% of the erosion yield of Kapton H), respectively. Therefore, a 20 µm thick CNT–15 wt% POSS–PI film is anticipated to function for more than 10 years in LEO.

The change in electrical resistivity of CNT–POSS–PI films as a function of AO fluence is drawn in Figure 5d. The resistivity of the CNT–PI film increased considerably upon exposure to AO, which can be explained by damage to the conductive CNT network. However, the CNT–POSS–PI films (5 and 15 wt% POSS) exhibited an almost constant electrical resistivity after AO attack, thanks to the AO-induced passivation

layer that protected the CNT network. Overall, the addition of POSS to the CNT–PI films establishes a novel class of *self-passivating* advanced materials resistant to both AO attack and ESD.

The morphology of the eroded CNT–POSS–PI films is shown in **Figure 6**.[93] The PI matrix of POSS-free films exposed to AO fluence of 6.0×10^{19} O-atoms cm^{-2} was eroded, leaving a somewhat damaged bare CNT network (Figure 6a) due to the higher erosion yield of PI compared to CNTs. Although relatively AO resistant, the CNTs were damaged, as indicated by the truncated CNTs. Figure 6b,c, respectively, shows HRSEM images of the CNT–POSS–PI films with 5 and 15 wt% POSS after exposure to the same AO fluence. These images reveal a different erosion pattern compared to the CNT–PI film, which is characterized by clusters rather than bare nanotubes. The CNT–POSS–PI films exposed to 2.3×10^{20} O-atoms cm^{-2} (5 and 15 wt% POSS, Figure 6e,f, respectively) show a similar clustered structure, and appear black in the macroscopic images (insets). Both 5 wt% and 15 wt% POSS-containing films demonstrate larger clusters as the AO fluence is increased. On the other hand, the CNT–PI film exposed to the same fluence (2.3×10^{20} O-atoms cm^{-2}) appears yellowish-brown in the macroscopic image (see inset), indicating a complete erosion of the CNT–PI layer

**ADVANCED
SCIENCE NEWS**

www.advancedsciencenews.com

**ADVANCED
MATERIALS**

www.advmat.de
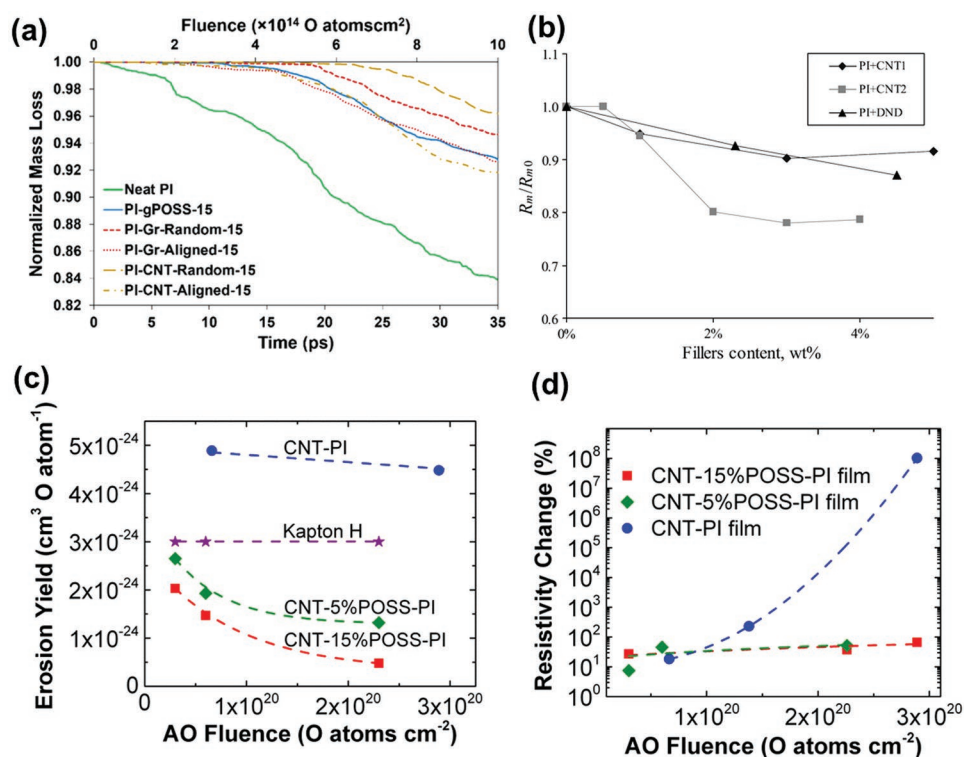
Figure 5. Influence of AO exposure on PI-based nanocomposites. a) Reactive molecular dynamics simulation of the normalized mass loss for both pristine PI and PI–POSS, as well as randomly oriented and aligned graphene and CNT nanoparticles (15 wt%). Reproduced with permission.[66] Copyright 2017, American Chemical Society. b) Calculated reduction in mass erosion yield as a function of filler content for PI composites with bare MWCNTs (PI-CNT1), functionalized MWCNTs (PI-CNT2), and DNDs as fillers. Reproduced with permission.[120] Copyright 2016, American Institute of Aeronautics and Astronautics. c) Erosion yields of CNT–POSS–PI films (0, 5, and 15 wt% POSS content) and Kapton H as a function of AO fluence. Reproduced with permission.[93] Copyright 2015, American Chemical Society. d) Electrical sheet resistivity changes of CNT–POSS–PI films (0, 5, and 15 wt% POSS content) as a function of AO fluence. Reproduced with permission.[93] Copyright 2015, American Chemical Society.

(Figure 6d), showing the remaining PI layer (and no apparent CNTs). The CNT–POSS–PI cluster formation resulting from oxidation of the POSS is characterized by a change in the Si:O atomic ratio, from 2:3 (in POSS) to 1:2 in SiO_2. The so-formed SiO_2 serves as a stable protective layer against AO attack.

5. 3D Polyimide Structures

5.1. Thermoforming

Thermoforming is an innovative approach, targeting the production of lightweight space-qualified mechanisms. It is based on transformation of 2D PI films into 3D structures by means of a thermal treatment.[122] This novel process can expand the use of PI toward new space applications, such as lightweight springs and actuators. **Figure 7**a shows 3D thermoformed helical, angular, and cylindrical shapes that can be further used as PI-based moving mechanisms. Since space-qualified systems may be stowed for extended periods during integration and preparation for launching, the dimensional stability of the thermoformed PI elements is of major interest. Accelerated creep under aging conditions was investigated.[122] Figure 7b demonstrates the creep-strain kinetics of thermoformed PI

films at RT, 40, and 65 °C. The empirical Findley power law was employed to envisage the creep strain versus time behavior of thermoformed Kapton.[123] The creep tests were conducted during an extended period of about 160 days. During the first two days, the creep strain instantly increased to 30–40%. After about 160 days, the final creep values of the thermoformed PI were 45–55%. This creep data can be used in concrete engineering design of novel devices.

5.2. Additive Manufacturing

Additive manufacturing (AM, also known as 3D Printing) is a process of depositing materials, typically layer by layer, to manufacture items from a 3D computer-aided design (CAD) model. Materials and processes for space applications raise several challenges, including low mass requirement, small production series, challenging material procurement, very high performances, and very high reliability. AM is well-suited for space applications: it is adaptive to very small series, applicable to dimensions ranging from tens of micrometers to meters, applicable to a wide variety of materials (polymers, metals, ceramics, composites, tissues and living cells, food for astronauts, etc.), allows for complex geometries that could not be manufactured before, enables reduction of interfaces (e.g., flanges, connectors,

**ADVANCED
SCIENCE NEWS**

www.advancedsciencenews.com

**ADVANCED
MATERIALS**

www.advmat.de
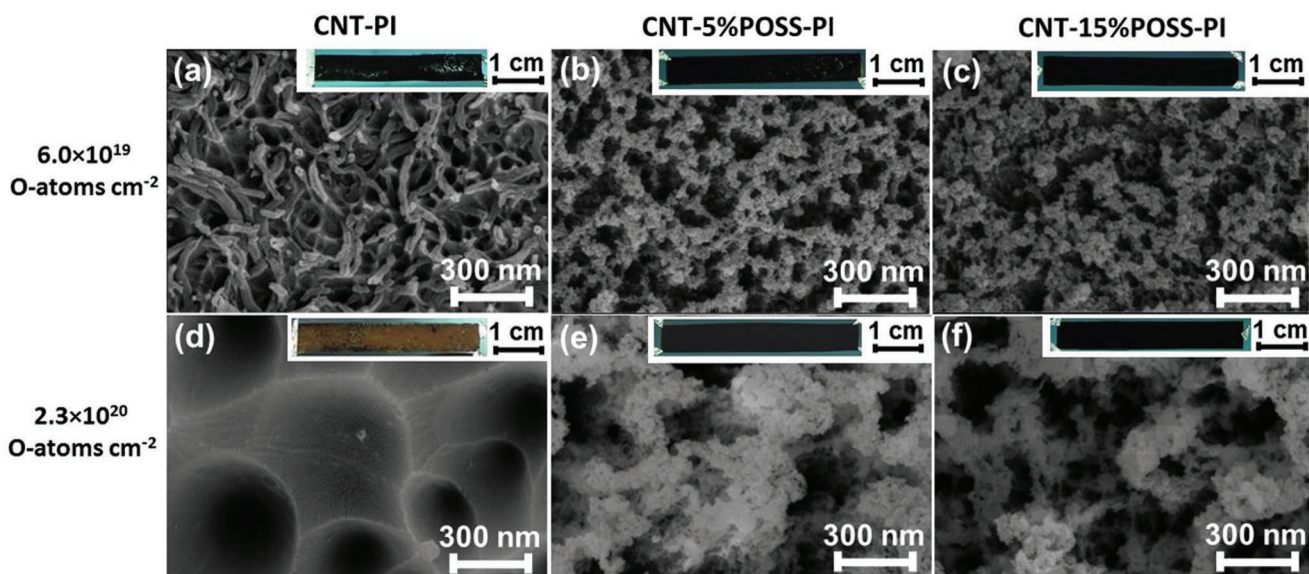
Figure 6. HRSEM images of CNT–POSS–PI films (0, 5, and 15 wt% POSS content) exposed to LEO equivalent AO fluences of 6.0×10^{19} and 2.3×10^{20} O-atoms cm^{-2} (macroscopic images as insets). All panels reproduced with permission.[93] Copyright 2015, American Chemical Society.
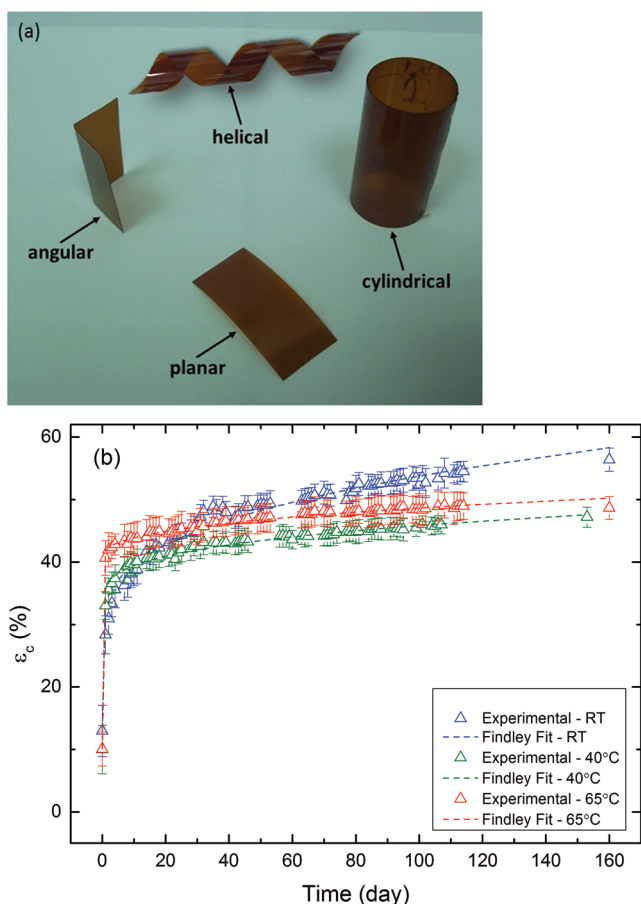
Figure 7. a) Planar PI film thermoformed into helical, angular, and cylindrical profiles. b) Creep strain kinetics of thermoformed PI films at various temperatures. All panels reproduced with permission.[122] Copyright 2016, Elsevier.

cables), allows significant mass reduction, provides performance improvement, short lead time, minimal material waste, and could be used for spacecraft construction and even for in-orbit manufacturing.[124]

Thus, AM can be regarded as an enabling technology for future space missions. A recent report[125] is predicting that the annual value of AM parts in the space industry will reach $4.7 billion, driving nearly $1 billion in yearly sales of 3D-printing equipment, software, and materials. Space applications may include, but are not limited to, RF hardware, antenna components, support elements for solar panels, turbine blades, thruster nozzles, lightweight structures (e.g., diffusion bonded titanium honeycomb), joint elements, electronics housing and mounting, and fabrication and assembly of large space structures in space or on other planetary surfaces. NASA already is testing a 3D printer on board of the International Space Station.[124,126,127] In addition, AM is expected to play a significant role in future planetary exploration missions, such as the "Moon Village," a concept proposed by ESA of a village on the Moon built by massive 3D printers and populated for months at a time by crews of astronauts. However, before AM can be widely used in space programs, multiple challenges should first be resolved, including development of space-qualified printable materials.

The use of polymers in space applications has obvious advantages. However, at present, the choice of AM-processable polymers is relatively limited. All materials going into space must have the ability to endure temperatures that may vary from −100 to +100 °C. Fused deposition modeling (FDM) technology uses a filament that is melted down and extruded from a print head. Currently, mostly thermoplastic filaments are used as feedstock in FDM, including acrylonitrile butadiene styrene (ABS), polycarbonate (PC), polylactide acid (PLA), polyamide (PA), and polyetherimide (PEI). Melt-processable thermoplastic polyimides were also printed using FDM and laser sintering (LS).[128–130] Recently, Chuang et al. investigated

LS of thermosetting RTM370 imide resin aiming to produce objects with high service temperatures (250–300 °C).[128] Yet, current material offerings, such as ABS-ESD7 and ULTEM 9085, do not meet all the requirements for space applications simultaneously. Therefore, there is a need for new, advanced polymers for AM. In this line, Stratasys has collaborated with industrial partners to develop ESD polyether ketone ketone (PEKK). ESD-PEKK combines the electrostatic dissipative properties from ABS-ESD7 and the strength and thermal properties of ULTEM 9085 with the addition of the PEKK base resin's chemical resistance. This polymer meets outgassing requirements.[131]

Optomec has a powerful technology for 3D printing of electronics—the Aerosol Jet. This process uses aerodynamic focusing to precisely and accurately deposit nanoparticle inks onto substrates. NASA is investigating the use of this technology to construct densely populated electronic (detector) assemblies that are not possible with traditional assembly processes. Optomec is currently developing also adaptive laser sintering system (ALSS), which will enable electronics' 3D printing onto a broader range of temperature-sensitive substrates, explicitly for use on board of the ISS in microgravity settings.[132]

PolyJet 3D printing by Stratasys operates similarly to inkjet printing, but instead of jetting drops of ink onto paper, PolyJet printers jet layers of liquid photopolymers onto a build tray, which are then cured by UV light. PolyJet's ability to create parts of great complexity and use multiple materials makes it useful for concept models. Engineering polymers, especially polyimides with their unique mechanical, thermal, and electrical insulating characteristics, are not commonly used as inks in inkjet AM technology. Our recent studies resulted in a groundbreaking development of low viscosity, high solid content, and environmentally friendly PI-based ink for PolyJet 3D printing.[133–135] This innovative ink solution was characterized in terms of viscosity, uniformity, surface tension, safety, and stability. The solution was found to fit the constraints and requirements of the PolyJet technology, while the final product retained PI-specific high thermal stability. The viscosities of PI-like ink solutions (60 and 80 wt% solid content) were measured, as displayed in **Figure 8**a. The viscosity of the PI-like ink, around 20 cP, fits the requirements at temperatures lower than or similar to the target jetting temperature (50–70 °C). The jetting and printing at a relatively low temperature is a great advantage since it allows multi-materials printing simultaneously. During the heating process, the PI-like ink exhibits an exothermic reaction at around 320 °C. After postcuring at temperatures of up to 400 °C, the film exhibits thermosetting characteristics. The novel PI-like ink was tested using a Stratasys 3D printer (Objet500 Connex). For
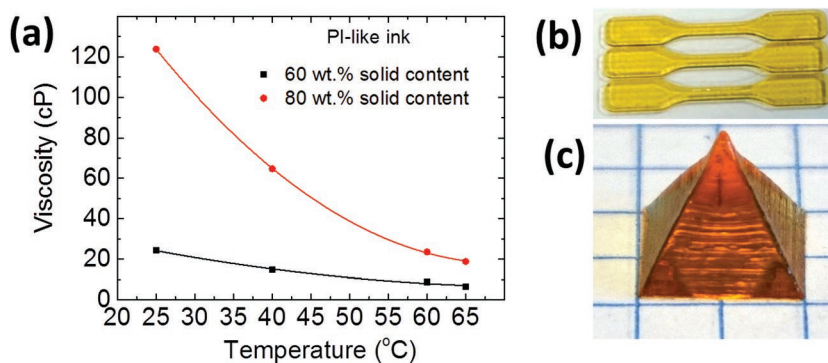
Figure 8. a) Viscosity versus temperature of PI-like ink solutions (60 and 80 wt% solid content).[133–135] b) Printed film in a dog-bone shape. c) 1 cm high pyramid printed from a solution with 80 wt% solid content using a Stratasys 3D Objet500 Connex printer.

the first time, thermally stable PI-like objects were obtained using the PolyJet Technology (see a printed dog bone sample, Figure 8b, and a 1 cm high pyramid Figure 8c). This new ink has great potential for manufacturing complex and lightweight parts durable and qualified for space applications. The printed objects retained PI-specific high thermal stability and high strength, very low outgassing, and radiation durability. Improved physical properties may be obtained by addition of either nanoparticles (e.g., nanotubes, nanodiamonds, or carbon black) or additives of reactive monomers, such as aromatic bismaleimides, acrylates, or epoxies.

A few other examples of printing PIs, not necessarily targeted to space applications, have been published. Zhang et al.[136] reported the continuous processing of inkjet-printed insulating PI thin films, used as insulating layers in capacitors. The PI ink was prepared from its precursor polyamic acid, and directly printed onto a hot substrate (at around 160 °C) to initialize a rapid thermal imidization. Guo et al.[137] developed novel photosensitive PI inks for digital light processing (DLP) AM. They used maleic anhydride-terminated PI oligomer grafted with glycidyl methacrylate groups in the chain as a base, vinyl pyrrolidone, lauryl methacrylate, and polyethylene glycol diacrylate as reactive diluents, and IRGACURE 819 as a photoinitiator. The decent solubility of the oligomers in reactive diluents enabled the formation of a solvent-free photocurable ink for DLP AM. O'Keefe et al.[138] synthesized low-k dielectric

Figure 9. Images of complex, anisotropic 3D structures immediately after printing, using mask-projection micro-stereolithography (MPμSL). The 3D structures contain 85 wt% N-methyl-2-pyrrolidone (NMP) solvent. Reproduced with permission.[139] Copyright 2017, Wiley-VCH.

**ADVANCED
SCIENCE NEWS**

www.advancedsciencenews.com

**ADVANCED
MATERIALS**

www.advmat.de

nanoparticles consisting of a polytetrafluoroethylene (PTFE) core and a PI shell for AM of microwave devices. A solution processed through the electrostatic interaction between PTFE with negative potential and polyamic acid salt (PAAS, a PI precursor) with positive potential, followed by thermal imidization of PAAS, was used. Hegde et al.[139] demonstrated 3D printing of all-aromatic thermoplastic PMDA–ODA PI using mask-projection stereolithography, and the preparation of high-resolution 3D structures without sacrificing bulk material properties. Synthesis of a soluble precursor polymer containing photo-crosslinkable acrylate groups enabled light-induced, chemical crosslinking for spatial control in the gel state. Post-printing thermal treatment transformed the crosslinked precursor polymer to PMDA–ODA. Large-area mask-projection scanning stereolithography demonstrated the scalability of 3D structures. **Figure 9** shows "high-resolution" 3D structures fabricated by a custom mask-projection micro-stereolithography machine. The layer thickness in this case is 100 μm, and the resolution is on the micrometer scale.

The same group later demonstrated AM of all-aromatic PI employing stereolithographic AM of PAAS.[140] In this system, 2-(dimethylamino)ethyl methacrylate (DMAEMA) interacted electrostatically with the PAA backbone, yielding UV-sensitive PAA DMAEMA salts. Under UV irradiation, TPO initiated crosslinking of DMAEMA, generating an organogel. After printing, heating the organogel rendered all-aromatic PMDA–ODA PI, which was thermally stable at as high as 500 °C.

Polyakov et al.[141] prepared by FDM samples of both pure polyetherimide and polyetherimide with carbon nanofibers. Introduction of 1 wt% of nanofibers led to increase in the strength and elastic modulus of the printed samples, approaching modulus of samples obtained by injection molding. Rinaldi et al.[142] prepared a composite material based on polyetherimide, a high-performance thermoplastic PI, as matrix, and natural diatomaceous earth, either uncalcined or calcined, as filler. Uncalcined diatomite was also amino-functionalized by aminopropyldiethoxymethylsilane (APDEMS), in order to increase its chemical compatibility with the matrix. Mechanical testing showed a progressive increment of the Young's modulus with the filler content, while the tensile strength remained comparable to that of plain PEI. The composition based on 5 wt% of diatomite was selected as the optimal one for composites to be potentially applied by the FDM AM process.

6. Conclusions

The use of materials in space presents an ongoing challenge due to longer space missions, which require sustainable materials with improved properties and enhanced durability in extreme space environment. Major space hazards include hyperthermal AO, UV and ionizing radiation, electrical charging, and hypervelocity impact. This progress report focuses on extending the survivability in LEO and improving the performance of PI-based materials. The durability of PIs in AO is successfully increased by addition of POSS and formation of self-passivating materials. Addition of CNTs and graphene to PIs results in formation of conductive nanocomposites suitable for space applications. AM or thermoforming

of 3D PI structures allows combining the inherently attractive properties of PIs with manufacturing freedom. A novel PI-based material processed by the PolyJet technology is demonstrated.

Conflict of Interest

The authors declare no conflict of interest.

Keywords

[1] A. C. Tribble, *The Space Environment: Implementation for Spacecraft Design*, Princeton University Press, Princeton, NJ **1995**.

[2] E. Grossman, I. Gouzman, *Nucl. Instrum. Methods Phys. Res., Sect. B* **2003**, *208*, 48.

[3] E. Grossman, I. Gouzman, R. Verker, *MRS Bull.* **2010**, *35*, 41.

[4] B. A. Banks, D. L. Edwards, I. Gouzman, E. Grossman, Y. Kimoto, J. I. Kleiman, S. K. R. Miller, T. K. Minton, M. Tagawa, A. P. Tighe, M. Van Eesbeek, R. Verker, C. G. Zimmermann, *MRS Bull.* **2010**, *35*, 12.

[5] E. M. Silverman, *Space Environmental Effects on Spacecraft—LEO Material Selection Guide*, NASA Contractor Report No. 4661, Langley Research Center, Hampton, VA **1995**.

[6] S. Katz, E. Grossman, in *Wiley Encyclopedia of Composites* (Eds: L. Nicolais, A. Borzacchiello), 2nd ed., Vol. 5, John Wiley & Sons, New York **2012**, p. 2779.

[7] R. M. Reddy, *J. Mater. Sci.* **1995**, *30*, 281.

[8] I. Gouzman, E. Grossman, M. Murat, Y. Noter, N. Saar, G. Zilberman, T. K. Minton, D. J. Garton, D. Buczala, A. Brunsvold, *Eur. Space Agency [Spec. Publ.] SP-540* **2003**, 487.

[9] A. Laikhtman, I. Gouzman, R. Verker, E. Grossman, *J. Spacecr. Rockets* **2009**, *46*, 236.

[10] K. L. Bedingfield, R. D. Leach, M. B. Alexander, *NASA Reference Publication 1390*, NASA, Marshall Space Flight Centre, Huntsville, AL **1996**.

[11] A. de Rooij, in *Encyclopedia of Aerospace Engineering* (Eds: R. Blockley, W. Shyy), John Wiley & Sons, New York **2010**.

[12] B. Banks, *Spacecraft Polymers Atomic Oxygen Durability Handbook*, NASA-HDBK-6024, NASA, Washington, DC **2014**.

[13] *Orbital Debris Quarterly News*, Vol. 22, NASA, Huston, TX February **2018**, p. 11.

[14] D. J. Kessler, R. C. Reynolds, P. D. Anz-Meador, *Orbital Debris Environment for Spacecraft Designed to Operate in Low Earth Orbit*, NASA TM-100471, NASA Johnson Space Center, Houston, TX **1988**.

[15] R. J. Iredale, C. Ward, I. Hamerton, *Prog. Polym. Sci.* **2017**, *69*, 1.

[16] C. Murphy, *Polyimides: Synthesis, Applications and Research*, Nova Science Publishers, New York **2016**.

[17] M. K. Ghosh, K. L. Mittal, *Polyimides: Fundamentals and Applications*, Marcel Dekker, New York **1996**.

[18] T. Yamashita, F. Kodera, M. Mino, Y. Matsuzawa, K. Okano, in *Technical Proc. Nanotechnology Conf. Expo 2012: Volume 1: Advanced Materials, CNTs, Films and Composites*, CRC Press, Boca Raton, FL **2012**.

[19] D. Wilson, H. D. Stenzenberger, P. M. Hergenrother, *Polyimides*, Chapman and Hall, New York **1990**.

[20] *Polyimides: Synthesis, Characterization, and Applications*, (Ed: K. L. Mittal), Springer Science+Business Media, New York **1984**.

[21] A. Georgiev, D. Dimov, E. Spassova, J. Assa, P. Dineff, G. Danev, in *High Performance Polymers—Polyimides Based—From Chemistry to Applications* (Ed: M. J. M. Abadie), IntechOpen, Rijeka, Croatia **2012**.

[22] R. Yokota, *J. Photopolym. Sci. Technol.* **1999**, *12*, 209.

[23] M. Kaltenbrunner, T. Sekitani, J. Reeder, T. Yokota, K. Kuribara, T. Tokuhara, M. Drack, R. Schwödiauer, I. Graz, S. Bauer-Gogonea, S. Bauer, T. Someya, *Nature* **2013**, *499*, 458.

[24] D.-J. Liaw, K.-L. Wang, Y.-C. Huang, K.-R. Lee, J.-Y. Lai, C.-S. Ha, *Prog. Polym. Sci.* **2012**, *37*, 907.

[25] H. Gao, L. Huang, X. Lan, L. Liu, Y. Liu, J. Leng, *Proc. SPIE* **2017**, *10165*, 101651B.

[26] H. Gao, X. Lan, L. Liu, X. Xiao, Y. Liu, J. Leng, *Smart Mater. Struct.* **2017**, *26*, 095001.

[27] X. Xiao, D. Kong, X. Qiu, W. Zhang, Y. Liu, S. Zhang, F. Zhang, Y. Hu, J. Leng, *Sci. Rep.* **2015**, *5*, 14137.

[28] H. Koerner, R. J. Strong, M. L. Smith, D. H. Wang, L.-S. Tan, K. M. Lee, T. J. White, R. A. Vaia, *Polymer* **2013**, *54*, 391.

[29] L. Santo, F. Quadrini, A. Accettura, W. Villadei, *Proc. Eng.* **2014**, *88*, 42.

[30] T. K. Minton, D. J. Garton, in *Chemical Dynamics in Extreme Environments* (Ed: R. A. Dressler), World Scientific Publishing, Singapore **2001**, p. 420.

[31] J. A. Dodd, P. M. Baker, E. S. Hwang, D. Sporleder, J. A. Stearns, S. D. Chambreau, M. Braunstein, P. F. Conforti, *Rev. Sci. Instrum.* **2009**, *80*, 093104.

[32] M. Tagawa, K. Yokota, N. Ohmae, H. Kinoshita, *High Perform. Polym.* **2000**, *12*, 53.

[33] S. K. Rutledge, J. A. Mihelcic, *Surf. Coat. Technol* **1989**, *39–40*, 607.

[34] B. A. Banks, A. Snyder, S. K. Miller, K. K. De Groh, R. Demko, *J. Spacecr. Rockets* **2004**, *41*, 335.

[35] Y. Huang, X. Tian, S. Lv, S. Yang, R. K. Y. Fu, P. K. Chu, J. Leng, Y. Li, *Appl. Surf. Sci.* **2011**, *257*, 9158.

[36] A. Snyder, K. K. de Groh, *NASA-TM-210596 2001*, NASA, Arachon, France.

[37] J. Herrero, C. Guillén, *Vacuum* **2002**, *67*, 611.

[38] K. Gotlib-Vainstein, I. Gouzman, O. Girshevitz, A. Bolker, N. Atar, E. Grossman, C. N. Sukenik, *ACS Appl. Mater. Interfaces* **2015**, *7*, 3539.

[39] I. Gouzman, O. Gershevitz, E. Grossman, N. Eliaz, C. N. Sukenik, *AIP Conf. Proc.* **2009**, *1087*, 391.

[40] I. Gouzman, O. Girshevitz, E. Grossman, N. Eliaz, C. N. Sukenik, *ACS Appl. Mater. Interfaces* **2010**, *2*, 1835.

[41] T. K. Minton, B. Wu, J. Zhang, N. F. Lindholm, A. I. Abdulagatov, J. O'Patchen, S. M. George, M. D. Groner, *ACS Appl. Mater. Interfaces* **2010**, *2*, 2515.

[42] Y. Man, Z. Li, M. Shu, K. Liu, H. Liu, Y. Gao, *Surf. Interface Anal.* **2017**, *49*, 843.

[43] M. Qian, V. J. Murray, W. Wei, B. C. Marshall, T. K. Minton, *ACS Appl. Mater. Interfaces* **2016**, *8*, 33982.

[44] A. L. Brunsvold, T. K. Minton, I. Gouzman, E. Grossman, R. Gonzalez, *High Perform. Polym.* **2004**, *16*, 303.

[45] S. J. Tomczak, V. Vij, D. Marchant, T. K. Minton, A. L. Brunsvold, M. E. Wright, B. J. Petteys, A. J. Guenthner, G. R. Yandek, J. Mabry, *Proc. SPIE* **2006**, *6308*, 630804.

[46] R. Verker, E. Grossman, N. Eliaz, *Compos. Sci. Technol.* **2012**, *72*, 1408.

[47] R. Verker, E. Grossman, I. Gouzman, N. Eliaz, *Compos. Sci. Technol.* **2009**, *69*, 2178.

[48] R. Verker, *Ph.D. Thesis*, Tel-Aviv University, Israel, **2011**.

[49] X.-F. Lei, M.-T. Qiao, L.-D. Tian, P. Yao, Y. Ma, H.-P. Zhang, Q.-Y. Zhang, *Corros. Sci.* **2015**, *90*, 223.

[50] X. Li, A. Al-Ostaz, M. Jaradat, F. Rahmani, S. Nouranian, G. Rushing, A. Manasrah, H. Alkhateb, Miria Finckenor, J. Lichtenhan, *Eur. Polym. J.* **2017**, *92*, 233.

[51] T. K. Minton, M. E. Wright, S. J. Tomczak, S. A. Marquez, L. Shen, A. L. Brunsvold, R. Cooper, J. Zhang, V. Vij, A. J. Guenthner, B. J. Petteys, *ACS Appl. Mater. Interfaces* **2012**, *4*, 492.

[52] R. Verker, N. Eliaz, I. Gouzman, S. Eliezer, M. Fraenkel, S. Maman, F. Beckmann, K. Pranzas, E. Grossman, *Acta Mater.* **2004**, *52*, 5539.

[53] R. Yamanaka, A. V. Gubarevich, E. Miyazaki, T. Yamaguchi, O. Odawara, *Int. J. Microgravity Sci. Appl.* **2017**, *34*, 340207.

[54] R. Verker, E. Grossman, I. Gouzman, N. Eliaz, *Polymer* **2007**, *48*, 19.

[55] R. Verker, E. Grossman, I. Gouzman, N. Eliaz, *High Perform. Polym.* **2008**, *20*, 475.

[56] R. Verker, E. Grossman, N. Eliaz, *Acta Mater.* **2009**, *57*, 1112.

[57] C.-M. Leu, Y.-T. Chang, K.-H. Wei, *Macromolecules* **2003**, *36*, 9122.

[58] G. Song, X. Li, Q. Jiang, J. Mu, Z. Jiang, *RSC Adv.* **2015**, *5*, 11980.

[59] Y. Kimoto, T. Fujita, N. Furuta, A. Kitamura, H. Suzuki, *J. Spacecr. Rockets* **2016**, *53*, 1028.

[60] S. Duo, Y. C. Chang, T. Liu, H. Zhang, *Phys. Procedia* **2013**, *50*, 337.

[61] X. F. Lei, Y. Chen, H. P. Zhang, X. J. Li, P. Yao, Q. Y. Zhang, *ACS Appl. Mater. Interfaces* **2013**, *5*, 10207.

[62] X. Lei, M. Qiao, L. Tian, Y. Chen, Q. Zhang, *Corros. Sci.* **2015**, *98*, 560.

[63] X. Lei, P. Yao, M. Qiao, W. Sun, H. Zhang, Q. Zhang, *High Perform. Polym.* **2014**, *26*, 712.

[64] K. Qi, G. Zhang, *Polym. Compos.* **2015**, *36*, 713.

[65] A. Rahnamoun, A. C. T. van Duin, *J. Phys. Chem. A* **2014**, *118*, 2780.

[66] F. Rahmani, S. Nouranian, X. Li, A. Al-Ostaz, *ACS Appl. Mater. Interfaces* **2017**, *9*, 12802.

[67] J. Azadmanjiri, V. K. Srivastava, P. Kumar, M. Nikzad, J. Wang, A. M. Yu, *J. Mater. Chem. A* **2018**, *6*, 702.

[68] J. A. Samareh, E. J. Siochi, *Nanotechnology* **2017**, *28*, 372001.

[69] W. Yuan, J. Che, M. B. Chan-Park, *Chem. Mater.* **2011**, *23*, 4149.

[70] S. M. Yuen, C. C. M. Ma, Y. Y. Lin, H. C. Kuan, *Compos. Sci. Technol.* **2007**, *67*, 2564.

[71] B. K. Zhu, S. H. Xie, Z. K. Xu, Y. Y. Xu, *Compos. Sci. Technol.* **2006**, *66*, 548.

[72] S. Rawal, J. Brantley, N. Karabudak, in *6th Int. Conf. Recent Advances Space Technol. (RAST)*, (Ed: M. Ilarslan), IEEE, Piscataway, NJ **2013**.

[73] http://www.nanocomptech.com/newsblog/nanocomp-reaches-new-frontiers-on-nasas-juno-mission, Miralon carbon-based advanced materials, (accessed: April 2018

[74] X. Jiang, Y. Bin, M. Matsuo, *Polymer* **2005**, *46*, 7418.

[75] C. Park, Z. Ounaies, K. A. Watson, R. E. Crooks, J. Smith, S. E. Lowther, J. W. Connell, E. J. Siochi, J. S. Harrison, T. L. S. Clair, *Chem. Phys. Lett.* **2002**, *364*, 303.

[76] J. Smith, J. Connell, D. Delozier, P. Lillehei, K. Watson, Y. Lin, B. Zhou, Y. P. Sun, *Polymer* **2004**, *45*, 825.

[77] J. G. Smith, D. M. Delozier, J. W. Connell, K. A. Watson, *Polymer* **2004**, *45*, 6133.

[78] P. C. Ma, N. A. Siddiqui, G. Marom, J. K. Kim, *Composites, Part A* **2010**, *41*, 1345.

[79] J. H. Du, J. Bai, H. M. Cheng, *eXPRESS Polym. Lett.* **2007**, *1*, 253.

[80] D. S. Hecht, L. Hu, G. Irvin, *Adv. Mater.* **2011**, *23*, 1482.

[81] J.-W. Zha, F. Sun, S.-J. Wang, D. Wang, X. Lin, G. Chen, Z.-M. Dang, *J. Appl. Phys.* **2014**, *116*, 134104.

[82] X. Liao, W. Ye, L. Chen, S. Jiang, G. Wang, L. Zhang, H. Hou, *Composites, Part A* **2017**, *101*, 50.

[83] Y. J. Jung, S. Kar, S. Talapatra, C. Soldano, G. Viswanathan, X. Li, Z. Yao, F. S. Ou, A. Avadhanula, R. Vajtai, S. Curran, O. Nalamasu, P. M. Ajayan, *Nano Lett.* **2006**, *6*, 413.

**ADVANCED
SCIENCE NEWS**

www.advancedsciencenews.com

**ADVANCED
MATERIALS**

www.advmat.de

[84] M. David-Pur, L. Bareket-Keren, G. Beit-Yaakov, D. Raz-Prag, Y. Hanein, *Biomed. Microdevices* **2014**, *16*, 43.

[85] P. C. P. Watts, S. M. Lyth, E. Mendoza, S. R. P. Silva, *Appl. Phys. Lett.* **2006**, *89*, 103113.

[86] E. J. Garcia, D. S. Saito, L. Megalini, A. J. Hart, R. G. Villoria, B. L. Wardle, *J. Nano Syst. Technol.* **2009**, *1*, 1.

[87] R. R. Mitchell, N. Yamamoto, H. Cebeci, B. L. Wardle, C. V. Thompson, *Compos. Sci. Technol.* **2013**, *74*, 205.

[88] A. M. Marconnet, N. Yamamoto, M. A. Panzer, B. L. Wardle, K. E. Goodson, *ACS Nano* **2011**, *5*, 4818.

[89] H. Peng, X. Sun, *Chem. Phys. Lett.* **2009**, *471*, 103.

[90] N. R. Raravikar, L. S. Schadler, A. Vijayaraghavan, Y. Zhao, B. Wei, P. M. Ajayan, *Chem. Mater.* **2005**, *17*, 974.

[91] E. Lahiff, C. Y. Ryu, S. Curran, A. I. Minett, W. J. Blau, P. M. Ajayan, *Nano Lett.* **2003**, *3*, 1333.

[92] N. Atar, E. Grossman, I. Gouzman, A. Bolker, Y. Hanein, *ACS Appl. Mater. Interfaces* **2014**, *6*, 20400.

[93] N. Atar, E. Grossman, I. Gouzman, A. Bolker, V. J. Murray, B. C. Marshall, M. Qian, T. K. Minton, Y. Hanein, *ACS Appl. Mater. Interfaces* **2015**, *7*, 12047.

[94] Z. Chen, W. Ren, L. Gao, B. Liu, S. Pei, H.-M. Cheng, *Nat. Mater.* **2011**, *10*, 424.

[95] X. Cao, Y. Shi, W. Shi, G. Lu, X. Huang, Q. Yan, Q. Zhang, H. Zhang, *Small* **2011**, *7*, 3163.

[96] A. Bello, K. Makgopa, M. Fabiane, D. Dodoo-Ahrin, K. I. Ozoemena, N. Manyala, *J. Mater. Sci.* **2013**, *48*, 6707.

[97] X. Zhang, K. K. Yeung, Z. Gao, J. Li, H. Sun, H. Xu, K. Zhang, M. Zhang, Z. Chen, M. M. Yuen, *Carbon* **2014**, *66*, 201.

[98] M. T. Pettes, H. Ji, R. S. Ruoff, L. Shi, *Nano Lett.* **2012**, *12*, 2959.

[99] J. A. Rogers, T. Someya, Y. Huang, *Science* **2010**, *327*, 1603.

[100] W. Wang, S. Guo, M. Penchev, I. Ruiz, K. N. Bozhilov, D. Yan, M. Ozkan, C. S. Ozkan, *Nano Energy* **2013**, *2*, 294.

[101] Y. Qin, Q. Peng, Y. Ding, Z. Lin, C. Wang, Y. Li, F. Xu, J. Li, Y. Yuan, X. He, Y. Li, *ACS Nano* **2015**, *9*, 8933.

[102] J. Kuang, L. Liu, Y. Gao, D. Zhou, Z. Chen, B. Han, Z. Zhang, *Nanoscale* **2013**, *5*, 12171.

[103] J. Jia, X. Sun, X. Lin, X. Shen, Y.-W. Mai, J.-K. Kim, *ACS Nano* **2014**, *8*, 5774.

[104] Y. Meng, H. Wu, Y. Zhang, Z. Wei, *J. Mater. Chem. A* **2014**, *2*, 10842.

[105] M. Yoonessi, J. R. Gaier, M. Sahimi, T. L. Daulton, R. B. Kaner, M. A. Meador, *ACS Appl. Mater. Interfaces* **2017**, *9*, 43230.

[106] M. Loeblein, A. Bolker, S. H. Tsang, N. Atar, C. Uzan-Saguy, R. Verker, I. Gouzman, E. Grossman, E. H. T. Teo, *Small* **2015**, *11*, 6425.

[107] W. Oh, T. J. Shin, M. Ree, M. Y. Jin, K. Char, *Macromol. Chem. Phys.* **2002**, *203*, 801.

[108] L.-C. Tang, Y.-J. Wan, D. Yan, Y.-B. Pei, L. Zhao, Y.-B. Li, L.-B. Wu, J.-X. Jiang, G.-Q. Lai, *Carbon* **2013**, *60*, 16.

[109] W. Dai, J. Yu, Z. Liu, Y. Wang, Y. Song, J. Lyu, H. Bai, K. Nishimura, N. Jiang, *Composites, Part A* **2015**, *76*, 73.

[110] W. Dai, J. Yu, Y. Wang, Y. Song, F. E. Alam, K. Nishimura, C.-T. Lin, N. Jiang, *J. Mater. Chem. A* **2015**, *3*, 4884.

[111] W. Yan, Y. Zhang, H. Sun, S. Liu, Z. Chi, X. Chen, J. Xu, *J. Mater. Chem. A* **2014**, *2*, 20958.

[112] P. C. Irwin, Y. Cao, A. Bansal, L. S. Schadler, in *Annual Report Conf. Electrical Insulation Dielectric Phenomena*, IEEE, Albuquerque, NM **2003**, pp. 120–123.

[113] T.-L. Li, S. L.-C. Hsu, *J. Phys. Chem. B* **2010**, *114*, 6825.

[114] T. Murakami, K. Ebisawa, K. Miyao, S. Ando, *J. Photopolym. Sci. Technol.* **2014**, *27*, 187.

[115] S.-H. Xie, B.-K. Zhu, J.-B. Li, X.-Z. Wei, Z.-K. Xu, *Polym. Test.* **2004**, *23*, 797.

[116] ECSS-E-ST-20-07C Rev. 1, *Space Engineering: Electromagnetic Compatibility, European Cooperation for Space Standardization (ECSS)*, Noordwijk, The Netherlands, 7 February **2012**.

[117] C. Godet, *Philos. Mag. B* **2001**, *81*, 205.

[118] L. Gan, A. Bolker, C. Saguy, R. Kalish, D. Tan, B. Tay, D. Gruen, P. Bruno, *Diamond Relat. Mater.* **2009**, *18*, 1118.

[119] C. Godet, *J. Non-Cryst. Solids* **2002**, *299–302*, 333.

[120] L. S. Novikov, V. N. Chernik, E. N. Voronina, K. B. Vernigorov, M. Y. Yablokova, *J. Spacecr. Rockets* **2016**, *53*, 1012.

[121] ASTM E2089-15, *Standard Practices for Ground Laboratory Atomic Oxygen Interaction Evaluation of Materials for Space Applications*, American Society for Testing and Materials, West Conshohocken, PA **2015**.

[122] R. Verker, M. Ozeri, A. Bolker, M. Loeblein, E. H. T. Teo, I. Gouzman, *Polym. Degrad. Stab.* **2016**, *134*, 237.

[123] A. Plaseied, A. Fatemi, *J. Reinf. Plast. Compos.* **2009**, *28*, 1775.

[124] *3D Printing in Space*, The National Academies Press, Washington, DC **2014**.

[125] V. Magan, Additive manufacturing in the space industry to reach $4.7 billion, http://www.satellitetoday.com/technology/2017/08/18/additive-manufacturing-space-industry-reach-4-7-billion/ (accessed: April 2018).

[126] T. Ghidini, The use of 3D printing for space applications, *Room: The Space Journal* **2016**, *1*, https://room.eu.com/article/the-use-of-3d-printing-for-space-applications (accessed: April 2018).

[127] M. Lisi, T. Ghidini, Additive manufacturing enables microwave components for space applications, Microwaves&RF **2017**, http://www.mwrf.com/print/13680 (accessed: April 2018).

[128] K. C. Chuang, T. Gornet, H. Koerner, presented at *The Composites and Advanced Materials Expo (CAMX)*, Anaheim, CA September **2016**, https://ntrs.nasa.gov/search.jsp?R=20160011504 (accessed: January 2019).

[129] W. Z. Wu, W. L. Ye, P. Geng, Y. L. Wang, G. W. Li, X. Hu, J. Zhao, *Mater. Lett.* **2018**, *229*, 206.

[130] L. Hu, R. W. Avalian, *US 2017/0355820 A1*.

[131] F. Calignano, D. Manfredi, E. P. Ambmbrosio, S. Biamino, M. Lombmbardi, E. Atzeni, A. Salmi, P. Minetola, L. Iuliano, P. Fino, *Proc. IEEE* **2017**, *105*, 593.

[132] B. Jackson, NASA awards Optomec contract supporting 3D printed electronics in space, http://3dprintingindustry.com/news/nasa-awards-optomec-contract-supporting-3d-printed-electronics-space-116777/ (accessed: April 2018).

[133] I. Gouzman, E. Grossman, N. Atar, R. Verker, A. Bolker, Y. Carmiel, E. R. Wallach, M. Pokrass, A. Wagner, presented at *Proc. 14th ISMSE & 12th ICPMSE*, Biarritz, France, October **2018**.

[134] A. Wagner, I. Gouzman, N. Atar, E. Grossman, M. Pokrass, A. Fuchsbauer, L. Schranzhofer, C. Paulik, *J. Appl. Polym. Sci.* **2018**, 47244.

[135] I. Gouzman, N. Atar, R. Verker, A. Bolker, E. Grossman, *WO/2018/011674 2018, PCT/IB2017/054054*.

[136] F. Zhang, C. Tuck, R. Hague, Y. He, E. Saleh, Y. Li, C. Sturgess, R. Wildman, *J. Appl. Polym. Sci.* **2016**, *133*, 43361.

[137] Y. X. Guo, Z. Y. Ji, Y. Zhang, X. L. Wang, F. Zhou, *J. Mater. Chem. A* **2017**, *5*, 8.

[138] S. O'Keefe, Y. L. Li, C. K. Luscombe, *J. Appl. Polym. Sci.* **2017**, *134*, 45335.

[139] M. Hegde, V. Meenakshisundaram, N. Chartrain, S. Sekhar, D. Tafti, C. B. Williams, T. E. Long, *Adv. Mater.* **2017**, *29*, 1701240.

[140] J. Herzberger, V. Meenakshisundaram, C. B. Williams, T. E. Long, *ACS Macro Lett.* **2018**, *7*, 493.

[141] I. V. Polyakov, G. V. Vaganov, V. E. Yudin, E. M. Ivan'kova, E. N. Popova, V. Y. Elokhovskii, *Mech. Compos. Mater.* **2018**, *54*, 33.

[142] M. Rinaldi, I. Cacciotti, T. Ghidini, L. Pambaguian, U. Lafont, V. Canala, V. Massarelli, F. Nanni, presented at *Proc. 5th CEAS Air & Space Conf. Proc., Paper No. 208*, (Ed: C. Hermans), Delft University of Technology, The Netherlands, September **2015**.